ADVANCED ENERGY MATERIALS
www.advenergymat.de

Anion Localization on Termini of a Non-Fullerene Acceptor Aids Charge Transport

*Junjun Guo, Martin V. Appleby, Kui Ding, Tong Shan, James Shipp, Igor V. Sazanovich, Dimitri Chekulaev, Zhuoran Qiao, Ricardo J. Fernández-Terán, Rachel Crespo Otero, Nicola Gasparini, Hongliang Zhong, Julia A. Weinstein, and Tracey M. Clarke**

Non-fullerene acceptors have revolutionised organic photovoltaics. However, greater fundamental understanding is needed of the crucial relationships between molecular structure and photophysical mechanisms. Herein, a combination of spectroscopic, morphology, and device characterization techniques are used to explore these relationships for a high-performing non-fullerene acceptor, anti-PDFC. It focuses on transient absorption spectroscopy across multiple timescales and ultrafast time-resolved vibrational spectroscopy to acquire the "holy grail" of simultaneous structural and dynamic information for anti-PDFC and its blend with the well-known conjugated polymer PM6. Most significantly, it is observed that the singlet exciton of anti-PDFC is localised on the perylene diimide central core of the molecule, but the radical anion is primarily localised on the fluorinated indene malonitrile terminal units (which are common to many state-of-the-art non-fullerene acceptors, including the Y6 family). This electron transfer from the central core to the termini of an adjacent molecule is facilitated by a close interaction between the termini and the central core, as evidenced by single crystal diffraction data and excited state calculations. Finally, the very efficient charge extraction measured for PM6:anti-PDFC photovoltaic devices may be correlated with this anion localization, enabling effective charge transport channels and thus enhancing device performance.

1. Introduction

The past few years have seen the advent of novel, high-efficiency non-fullerene acceptors (NFAs) for organic photovoltaics (OPV). Due to this, the OPV field is currently enjoying a renaissance, with power conversion efficiencies now approaching 20%.[1–3] NFAs possess several characteristics that enable the current high performances observed.[4,5] One critical aspect of NFAs is that they possess high absorptivities, in contrast to traditional fullerenes. This enables both donor and acceptor to effectively contribute to charge photogeneration by hole transfer from the acceptor, in addition to the standard electron transfer from the donor. Furthermore, several blends based on NFAs have been reported to undergo efficient charge photogeneration with a minimal energetic offset for either electron or hole transfer.[6–8] This ability, which enables reduced voltage

J. Guo, R. Crespo Otero, T. M. Clarke
Department of Chemistry
University College London
Christopher Ingold Building, London WC1H 0AJ, UK
E-mail: tracey.clarke@ucl.ac.uk

J. Guo
Industrial Catalysis Centre
Department of Chemical Engineering
Tsinghua University
Beijing 100084, China

M. V. Appleby, J. Shipp, D. Chekulaev, R. J. Fernández-Terán, J. A. Weinstein
Department of Chemistry
The University of Sheffield
Sheffield S3 7H, UK

M. V. Appleby
Paul Scherrer Institut
Forschungsstrasse 111, Villigen PSI 5232, Switzerland

The ORCID identification number(s) for the author(s) of this article can be found under https://doi.org/10.1002/aenm.202404926

DOI: 10.1002/aenm.202404926

K. Ding, T. Shan, H. Zhong
School of Chemistry and Chemical Engineering
Shanghai Jiao Tong University
Shanghai 200240, China

T. Shan
College of New Materials and New Energies
Shenzhen Technology University
Shenzhen 518118, China

J. Shipp
Department of Chemistry
Chevron Science Centre
University of Pittsburgh
219 Parkman Avenue, Pittsburgh, PA 15260, USA

I. V. Sazanovich
Central Laser Facility, Research Complex at Harwell
STFC Rutherford Appleton Laboratory, Harwell Campus
Didcot, Oxfordshire OX11 0QX, UK

Z. Qiao, N. Gasparini
Department of Chemistry and Centre for Processable Electronics
Imperial College London, White City Campus
82 Wood Lane, London W12 0BZ, UK

R. J. Fernández-Terán
Department of Physical Chemistry
University of Geneva
30 Quai Ernest-Ansermet, Geneva CH-1205, Switzerland

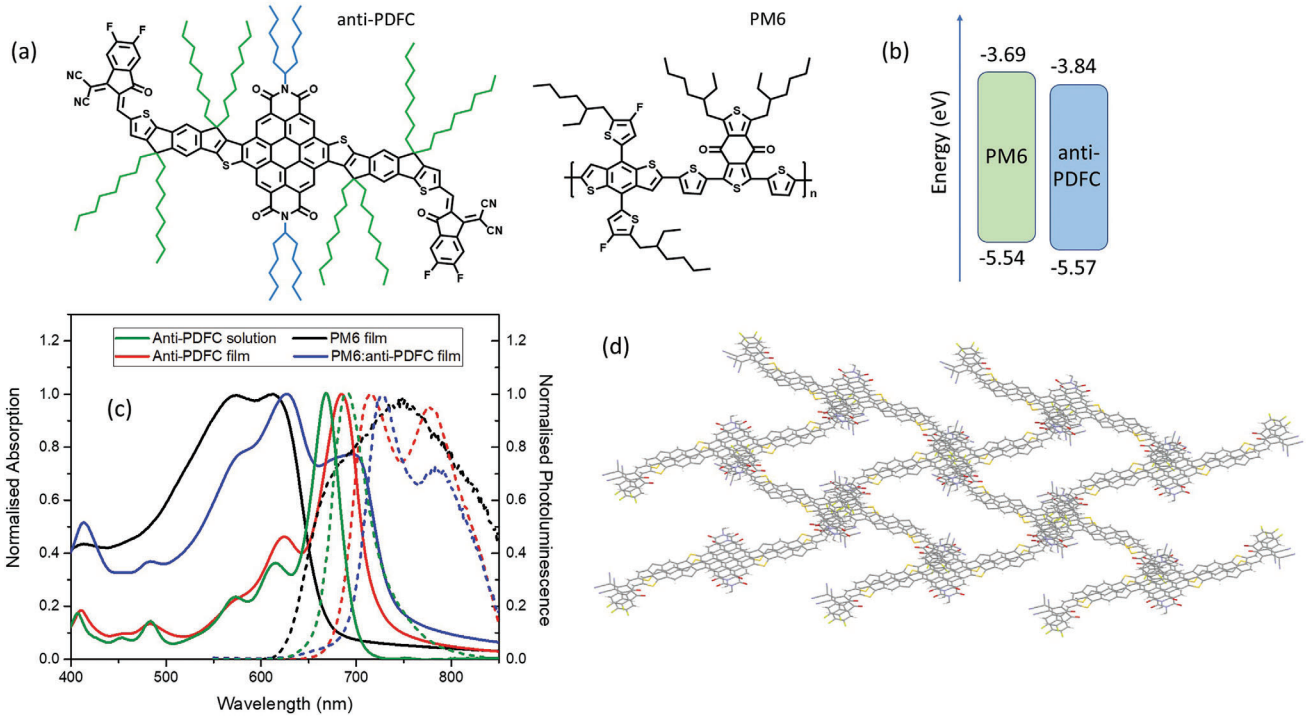

Figure 1. a) Molecular structures of anti-PDFC and PM6, b) the HOMO and LUMO energy levels of PM6 and anti-PDFC, as determined from their cyclic voltammograms and the relationship $LUMO = HOMO + S_1$, where the S_1 energy is estimated from the intersection point of normalised absorbance and emission spectra. c) Normalised steady-state absorption and photoluminescence spectra of pristine anti-PDFC film and chloroform solution, pristine PM6 film, and the PM6:anti-PDFC film (1:1.1). Solid lines denote absorption spectra, dashed lines denote photoluminescence spectra. d) Single crystal x-ray structure of anti-PDFC (excluding the hydrogens and alkyl chains), showing the stacking of the terminal and PDI groups to form a diamond motif.

losses, has been attributed to factors such as low reorganisation energies and large quadrupole moments. However, we lack information at the molecular level how non-fullerene acceptors can offer such high device performances and a more fundamental understanding is required to understand structure-function relationships in these materials. Most of the highest-performing NFAs, such as Y6, possess a similar A'-D-A-D-A' architecture, where the acceptor (A) and donor (D) moieties induce an alternating charge density "checkerboard pattern", which is enhanced due to the aggregation properties of NFAs.[9] Furthermore, fluorinated indene malonitrile (2FIC) terminal units have become ubiquitous in most recent NFA high-performers, including Y6. These have been reported to enhance intermolecular interactions,[10] form conformational locks to enhance crystallinity,[11] and push absorption further into the near-Infrared.[12–14]

To examine NFA processes at the molecular level, we require the "holy grail" of simultaneous structural and dynamic information of excited states on timescales relevant to OPV photophysical processes. Ultrafast time-resolved vibrational spectroscopy combines ultrafast dynamics information with high structural sensitivity. Small changes in geometry of hundredths of angstroms are detectable.[15] However, owing to the complexities of such experiments, the application of ultrafast vibrational spectroscopy to OPV systems is relatively limited to date. Despite this, numerous important advances in understanding have been achieved using such techniques. For example, Pensack *et al.* used time-resolved infrared spectroscopy to demonstrate that excess vibrational energy after electron transfer facilitates electrons escaping their Coulombic potentials on ultrafast time scales.[16] Falke *et al.* showed that coherent vibronic coupling between electronic and nuclear degrees of freedom helps induce both charge delocalization and transfer.[17] Femtosecond stimulated Raman spectroscopy has been used to observe that charge separation out-competes exciton localization[18] and shows how disorder affects vibrational coupling.[19] Such studies are excellent demonstrations of the power of ultrafast vibrational spectroscopy to provide extensive insight into OPV mechanisms.

Here we investigate the non-fullerene acceptor, anti-PDFC (**Figure 1a**). It possesses the A'-D-A-D-A' architecture common to many NFAs, with a perylene diimide (PDI) moiety flank fused with two indacenodithiophene units as the electron-donating moieties and two fluorinated indene malononitrile (2FIC) groups as the electron-withdrawing terminals. When blended with the high-performing polymer PM6 (poly[[4,8-bis[5-(2-ethylhexyl)-4-fluoro-2-thienyl]benzo[1,2-b:4,5-b″]dithiophene-2,6-diyl]-2,5-thiophenediyl[5,7-bis(2-ethylhexyl)-4,8-dioxo-4H,8H-benzo[1,2-c:4,5-c″]dithiophene-1,3-diyl]-2,5-thiophenediyl]), OPV device efficiencies of 12.6% with very high fill factors (FF) of up to 81% have been reported,[20] and up to 15.7% in ternary devices.[21] Herein, we use a combination of steady-state spectroscopy, spectroelectrochemistry, transient absorption spectroscopy (TAS) on multiple timescales, and ultrafast time-resolved infrared spectroscopy (TRIR) to delve into the photophysics of such a high fill factor system. Importantly, we also use it as a model

system to make critical links between photophysics and molecular structure. The TRIR has revealed that while the NFA singlet exciton is localised on the central core of the molecule, the radical anion is primarily localised on the 2FIC termini. This shift in excited state localization is facilitated by a close interaction between the PDI core and a 2FIC terminus in an adjacent molecule.

2. Results and Discussion

2.1. Steady-State Absorption and PL Spectroscopy

The normalized steady-state absorption spectra of the pristine polymer PM6, pristine anti-PDFC, and annealed blend PM6:anti-PDFC in films are displayed in Figure 1c. The absorption spectrum of the pristine anti-PDFC film is red-shifted compared to solution (in chloroform) and shows a narrow maximum at 685 nm; the small width of the peak is consistent with a relatively ordered morphology. Conversely, the pristine PM6 film shows equivalent intensity vibronic peaks at 615 nm and 575 nm, indicating a less crystalline structure. Blending the two components together induces a red-shift of the most intense anti-PDFC band from 684 nm to 695 nm, again suggesting an enhancement in order of the NFA component.[22,23] These changes are reflected even more strongly in the photoluminescence spectra. The PL of the anti-PDFC solution is essentially a single band, which alters to show a pronounced vibronic structure in the pristine film that is suggestive of a more rigorously ordered structure. The PL of the blend, however, is clearly more reminiscent of the NFA than the polymer; furthermore, the greater intensity ratio of the 0–0/0–1 vibronic peaks in the blend compared to the pristine anti-PDFC may suggest the presence of J-aggregation.[24]

2.2. Morphology Characterization

The morphology of the films was investigated via atomic force microscopy (AFM, Figure S1, Supporting Information) and grazing incidence X-ray diffraction (GIXRD, Figure S2, Supporting Information). The pristine PM6 film shows a needle-like structure with root-mean-square surface roughness Rq = 1.1 nm, suggesting a smooth surface. Pristine anti-PDFC NFA shows a much rougher surface, with Rq = 7.4 nm, but the annealed PM6:anti-PDFC film shows an intermediate Rq of 2.9 nm, which suggests some degree of miscibility between PM6 and anti-PDFC. However, the GIXRD suggests that the crystallinity of the anti-PDFC is minimally impacted by the presence of the PM6. The PM6 is clearly amorphous due to the lack of a π–π stacking peak in the GIXRD. The π–π stacking peak of anti-PDFC at $\approx$17 nm^{-1} reveals identical π–π d-spacing in both pristine anti-PDFC and the blend (0.37 nm). Furthermore, the size (coherence length) of the anti-PDFC crystallites, calculated using the broadness of the π–π stacking peak, also exhibits minimal changes from pristine to blend, increasing slightly from 7.1 $\pm$ 0.1 nm to 7.5 $\pm$ 0.1 nm.

The single crystal X-ray structure of anti-PDFC has been previously published[21] and shows a 3D reticular packing motif in a diamond configuration, where both sets of orthogonal alkyl chains enable a highly ordered lamellar packing structure. Furthermore, the C_{2h}-like symmetry of the anti-PDFC backbone facilitates a long-range helical structure across the lamellar planes.[25,26] Importantly, the crystal structure reveals an alternating π-stacking structure of the terminal units and the PDI core, as illustrated in Figure 1d and Figure S3 (Supporting Information), where the distance between the PDI plane and the centre of the terminal group is 3.42 Å. Although the molecular planes are not parallel, this small distance (noting that the estimated van der Waals radius of carbon is 1.7 Å[27]) implies a strong interaction. These close interactions between the electron-deficient moieties have been observed in single crystal X-ray structures of multiple other non-fullerene acceptors, including those that share the same 2FIC terminal group as anti-PDFC. ITIC[12] and IDTBR[28] derivatives typically show a close overlap between the terminal groups while Y6 shows more complex interactions, with overlaps between both cores and end groups.[29,30] In all cases, the close proximity of the electron-deficient moieties has been shown to lead to electronic coupling and thus may assist electron transport. As such, it is probable that the similarly close interaction between electron-deficient moieties in anti-PDFC has the same effect.

2.3. Transient Absorption Spectroscopy and Spectroelectrochemistry

A series of control samples (solutions and pristine films) were studied to ascertain electronic absorption peak positions for relevant excited states, such as charge carriers and triplet states; the results of these experiments are shown and discussed in the supporting information, Figures S4–S6 (Supporting Information). Having established the control spectra for expected excited states, the spectroscopic behaviour of the PM6:anti-PDFC film can now be assessed. Two excitation wavelengths were employed: 520 nm mainly excites the PM6 (although 520 nm corresponds to a minimum in the anti-PDFC absorption, some anti-PDFC absorption is still present at this wavelength) and 665 nm selectively excites the anti-PDFC. The µs-TA spectra are shown in **Figure 2**a, with both excitation wavelengths presenting three TA bands at <700 nm (peak position obscured by the ground state bleach), 900 nm, and a rising tail to beyond 1600 nm. It is immediately apparent that both the PM6 cation and anti-PDFC anion are present in the PM6:anti-PDFC blend spectra, given the close resemblance to the relevant control spectra. Also shown is a TA spectrum of PM6:PC60BM, revealing an absence of the rising tail to beyond 1600 nm. This observation helps verify that the >1600 nm band in the PM6:anti-PDFC blend must be attributed to the anti-PDFC anion rather than the PM6 cation. While the band at 900 nm is clearly the polymer cation, both donor and acceptor charge carriers have intensity below 700 nm and thus we can only assign the <700 nm band to charge carriers and cannot establish their identity. No evidence of triplet state formation or oxygen sensitivity of the blend's decay dynamics is observed (Figure S7, Supporting Information). It is also observed that the decay dynamics of the charge carriers (Figure S8, Supporting Information), are very rapid, with more than 90% of the charge carriers decaying prior to 3 µs.

When corrected for the number of photons absorbed (Figure S9, Supporting Information), we can assess relative polaron populations. For the 900 nm polymer polaron exciting at 520 nm,

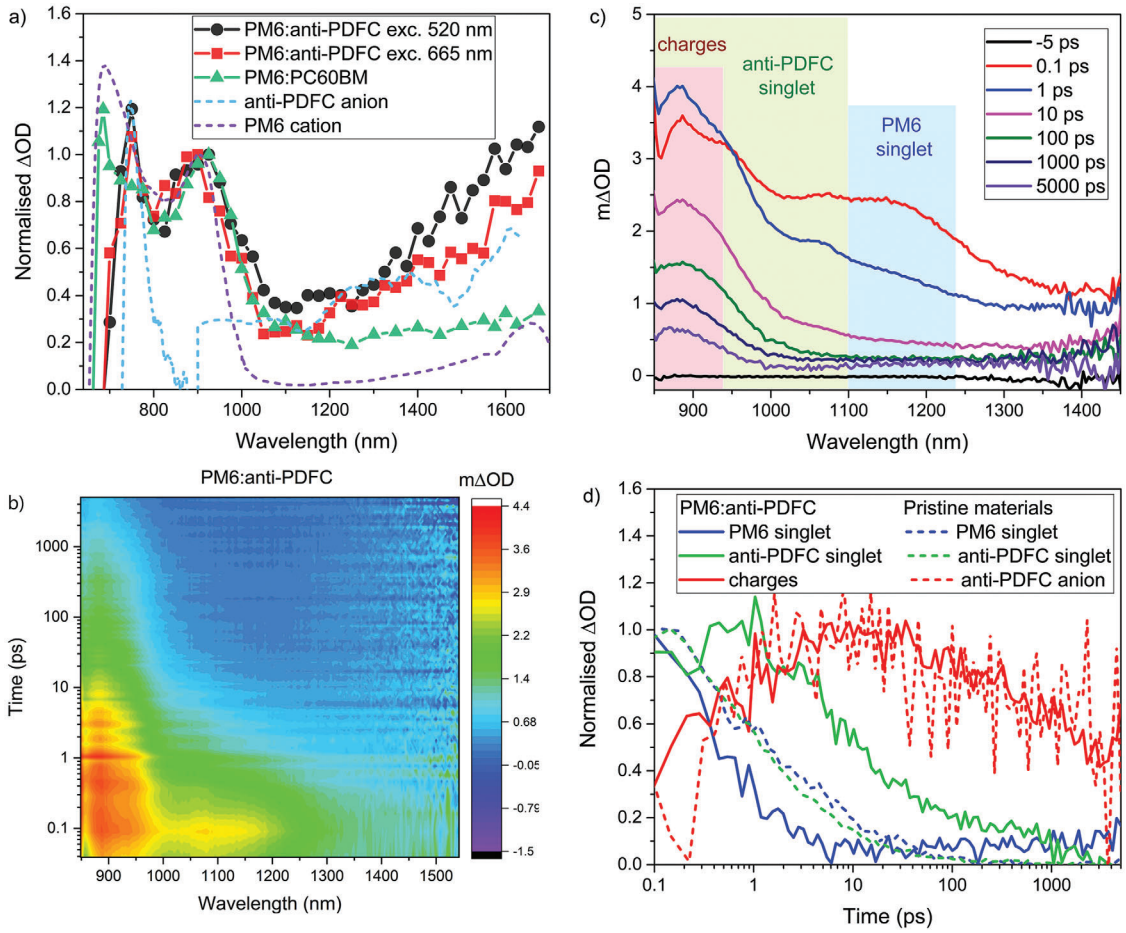

Figure 2. a) μs-TA spectra measured at 1 μs, normalised to 1 at the 900 nm polaron, for the PM6:anti-PDFC blend film exciting at both PM6 (520 nm) and anti-PDFC (665 nm), and compared to film control spectra of PM6:PC60BM, pristine PM6, and the SEC spectra. Excitation densities used were in the range 12–15 μJ cm^{-2}. b) Ultrafast transient absorption spectral colour map and c) raw spectra over time for the annealed PM6:anti-PDFC film. d) Ultrafast TAS kinetics extracted from global analysis, comparing the pristine materials (dashed lines) with the PM6:anti-PDFC blend film (solid lines). An excitation wavelength of 520 nm and 30 μJ cm^{-2} was used for the data shown in (b)–(d).

the PM6:anti-PDFC blend has ≈40% more charge carriers than PM6:PC60BM and ≈65% more charges than the pristine PM6 film. We can examine this further by looking at the population of the PM6 polaron with selective anti-PDFC excitation at 665 nm for the PM6:anti-PDFC blend. It can be observed that the 900 nm PM6 polaron population is a factor of 2.5 time greater with primarily PM6 excitation compared to selective anti-PDFC excitation. Interestingly, the kinetics of this 900 nm PM6 polaron in the PM6:anti-PDFC blend is similar to that in the pristine PM6 film. The kinetics can be fitted to a power law ($\Delta OD \propto t^{-\alpha}$) with an α of 0.8–1, attributed to fast, trap-free bimolecular recombination (Figure S8, Supporting Information). Furthermore, the decay dynamics are largely energy-independent. These results suggest the charge carrier recombination is likely dominated by that occurring within pure polymer domains.[31] This is consistent with the polaron populations observed, where there appears to be an additive effect: the TA amplitude of the 900 nm polaron in the PM6:anti-PDFC blend for selective anti-PDFC excitation combined with that of pristine PM6 is approximately equal to that seen for PM6:anti-PDFC blend with polymer excitation. The implication of this observation is that the total polymer polaron population in the blend results from both intrinsic charge photogeneration in the polymer and also hole transfer from the NFA.[9]

2.4. Ultrafast Transient Absorption Spectroscopy

Ultrafast TAS is employed to understand the charge generation and recombination processes in PM6:anti-PDFC in more detail, with the main results shown in Figure 2b–d. Pristine PM6 ultrafast TA data has been previously published several times,[32–34] but it is included here for completeness as an important control (Figure S10, Supporting Information). To that end, and using global analysis to extract individual spectral components and their accompanying kinetics (global analysis data is presented in Figure S11, Supporting Information), the pristine film PM6 singlet exciton occurs at 1150 nm. After the singlet exciton decays, the remaining TA signal resembles the PM6 positive polaron observed in both the μs-TAS and spectroelectrochemistry. On these ultrafast timescales, this remaining TA signal has been

previously assigned to bound polaron pairs, consistent with our results.[35,36]

The pristine anti-PDFC film (Figure S10, Supporting Information) shows a broad singlet exciton at ≈900 nm with vibronic structure, including a strong shoulder at 1050 nm. Although weak, a residual signal above 1400 nm exists on the early ns timescales that matches the anti-PDFC anion from spectroelectrochemistry and µs-TAS. Global analysis, using the singlet exciton (at 200 fs) as a reference (Figure S12, Supporting Information), reveals that the singlet exciton has a strongly excitation-dependent behaviour with decay time constants of 3 and 43 ps at the lowest fluence. However, the anti-PDFC anion TA signal is too weak at the lowest fluence to extract meaningful kinetics and thus its behaviour is assessed using an intermediate fluence of 30 µJ cm^{-2} (Figure 2d; Figure S11, Supporting Information). Under these conditions, the anti-PDFC anion shows a rise over time with a time constant of $\tau = 0.7$ ps and a maximum population occurring at ≈10 ps. The 0.7 ps rise time constant of the anion matches one of the time components of the anti-PDFC singlet exciton decay using this fluence ($\tau = 0.8$ ps). As such, this anion formation will be a significant contribution to the deviation of the singlet exciton decay from first order. The remaining 9.3 ps time component of the anti-PDFC singlet exciton is therefore likely to be attributed to relaxation back to the ground state. Note that the 0.8 ps time constant of the anti-PDFC singlet decay, attributed to charge carrier formation, composes a significant proportion of the overall decay (62%), suggesting that intrinsic photogeneration is relatively efficient in anti-PDFC. This is consistent with the observation that anti-PDFC anions are still visible on µs timescales.

Now that we have assessed the pristine film controls of both components, we can consider the PM6:anti-PDFC blend (Figure 2b–d, Supporting Information). An excitation wavelength of 520 nm was chosen to minimise anti-PDFC absorption. Despite this, the raw data shows at the earliest time contributions from both PM6 and anti-PDFC singlet excitons, including the characteristic feature at 1050 nm possessed only by the anti-PDFC singlet (Figure 2b). Over longer (nanosecond) timescales, the TA data shows evidence of the presence of charge carriers: PM6 polarons most clearly (at 900 nm), however there is likely contribution from anti-PDFC anions, which absorb at similar wavelengths. No signatures corresponding to PM6 or anti-PDFC triplet states were observed in either the raw data or the results from global analysis (see the triplet state control spectra in Figures S4c and S6a, Supporting Information). It should be noted that a variety of references were trialled for the global analysis (pristine donor singlet exciton, pristine acceptor singlet exciton, and both pristine singlet excitons), and the key conclusions remained the same.

The ps-TAS global analysis reveals a delayed decay of the anti-PDFC singlet exciton in the blend, which becomes substantially longer-lived ($\tau = 11$ ps and 800 ps) compared to the singlet exciton in pristine anti-PDFC ($\tau = 3$ ps and 43 ps, Figure 2d). In contrast, the PM6 singlet exciton lifetime in the blend ($\tau = 0.3$, 2 ps) has decreased compared to the pristine PM6 film. Considering that it is already known that higher charge densities are achieved in the blend compared to the pristine samples (this is evident in both µs- and ps-TAS), evidence of the initially photogenerated singlet exciton being quenched by electron/hole transfer is expected.[37–39] The fact that this is not observed for the anti-PDFC singlet may suggest rapid singlet exciton transfer from PM6 to anti-PDFC, noting that the PM6 S_1 state lies at 1.92 eV while that of anti-PDFC is at 1.77 eV (estimated from the intersection of normalised steady-state absorption and PL spectra). Singlet energy transfer has been commonly observed in polymer/NFA blends.[9,40] Furthermore, an equilibrium may exist between the singlets and charge transfer (CT) states such that the lifetime of the lower energy anti-PDFC singlet in the blend is prolonged, as has been observed in other NFA blends.[6,7,41]

Interestingly, the kinetics of the charge carriers in the blend mirrors those in the pristine anti-PDFC: a rise in population to reach a maximum at ≈10 ps, followed by a slow decay (Figure 2d). However, the rise time of the charge carriers in the blend (1.1 ps) is slower than in pristine anti-PDFC(0.7 ps). This observation is consistent with ultrafast singlet energy transfer taking place prior to charge generation, inducing a small delay to the growth of the charge carrier population. The similarity of the decay kinetics of the anion component between pristine anti-PDFC and the blend suggests that the anions are sequestered in the anti-PDFC domains and decay there alongside those intrinsically photogenerated.

Kinetic modelling[42] has been applied to the ultrafast TA data of the PM6:anti-PDFC data to acquire more insight. The details can be found in the supporting information (Figures S13 and S14; Table S1, Supporting Information). A good fit with minimal residuals has been achieved for a kinetic model involving an exciton/CT state equilibrium and singlet energy transfer. Note that the presence of both these mechanisms is feasible given the low energetic offsets between both HOMOS and LUMOs of PM6 and anti-PDFC, implying that the S_1 energies and CT state energy will be similar, with the S_1 energy of anti-PDFC (1.77 eV) slightly lower than PM6 (1.92 eV). From the kinetic model analysis, branching ratios between competitive processes can be assessed. Considering the PM6 singlet exciton, formation of CT states and energy transfer to anti-PDFC effectively outcompete return to the ground state, with only 2% of PM6 excitons following the latter pathway. This observation is consistent with the PL of the blend showing solely anti-PDFC features. Although the energy transfer is fast (with a time constant of 0.53 ps), charge carrier formation is even faster ($\tau = 0.29$ ps), with 63% of PM6 singlet excitons directly generating charge carriers. It is possible that the similarity between the S_1 energies of PM6 and anti-PDFC inhibit energy transfer since less of a driving force is present.

2.5. Time-Resolved Infrared Spectroscopy

Now that we have a clearer picture of the photophysics occurring in both the pristine materials and the blends, we turn to ultrafast infrared spectroscopy to gain more detailed structural information regarding these processes. To facilitate the analysis of such a complex system, the infrared spectrum for the ground state of anti-PDFC was calculated using density functional theory and compared to the experimental IR spectrum (Figures S15,S16a, Supporting Information). Of particular interest are marker modes: vibrational modes that are relatively isolated in terms of wavenumber (to minimise overlap between modes) and represent specific parts of the molecule. For

anti-PDFC, these markers include the C≡N stretch (2218 cm^{-1} in the ground state), far from any other vibrational modes, and the C═O stretches above 1600 cm^{-1}. In the case of anti-PDFC, the 1662 cm^{-1} peak is assigned to the C═O stretches on the perylene-diimide (PDI) core, while the 1701 cm^{-1} band has a dominant contribution from the 2FIC termini C═O stretch, although the PDI C═O stretch also contributes.

The TRIR spectra contain a very large, broad background due to an underlying signal from the electronic absorption. To extract the vibrational data only, we performed a standard baselining procedure, which involved fitting a polynomial function to the background and subtracting that function. The linearity of the TRIR signal was assessed as a function of power/fluence. A power of 1 mW (corresponding to a fluence of 1.1 mJ cm^{-2}) was chosen for the kinetic analysis as the best compromise between remaining in the linear regime and signal-to-noise considerations. As such, while the raw data is shown at 5 mW to maximise the visibility of the transient features in **Figure 3**, the baselined spectra and kinetics are shown at the lower power of 1 mW in **Figure 4**. More raw data, baselined data, and the fluence dependence are shown in Figures S17–S19 (Supporting Information).

The TRIR spectra for pristine anti-PDFC (Figures 3a and 4a; Figure S18, Supporting Information) are dominated by two very large ground state bleaches (GSBs) at 1420 and 1543 cm^{-1}. Both are related to the C═C bond linking the 2FIC terminal units to the rest of the molecule. Other clear GSBs are those at 1602 cm^{-1} (assigned to the 2FIC's fluorinated benzene stretch), the CN stretch at 2221 cm^{-1}, and the CO stretch at 1662 cm^{-1}. The 1662 cm^{-1} mode is accompanied by a broad excited state absorption (ESA) in the 1620–1660 cm^{-1} region. Indeed, according to literature reports of other TRIR studies of PDI-based compounds, this is the region we expect to see the PDI singlet state (and anion).[43–46]

We can assess the decay kinetics of these vibrational features (decay time constants shown in **Table 1**), but it should be noted that the often-overlapping nature of broad GSBs and ESAs can influence the observed kinetics. In Figure 4b, the decay kinetics of the pristine anti-PDFC's PDI core C═O stretch ESA at 1648 cm^{-1}, the terminal 2FIC's C≡N stretch bleach, and the 1602 cm^{-1} bleach (also relating to the 2FIC termini) are compared. It can immediately be observed that the ESA decay kinetics of the 1648 cm^{-1} mode related to the central PDI core of the anti-PDFC are quite different compared to those of the termini modes. In particular, the central PDI core C═O stretch (1648 cm^{-1}) decays rapidly, with lifetime components of 0.8 and 14 ps, and there is very little ESA remaining on the nanosecond timescales. In contrast, the termini vibrational modes have longer lifetime components of 2 and 25 ps. Indeed, it can be observed that the rapid decay kinetics of the 1648 cm^{-1} PDI C═O stretch ESA match very well with the extracted singlet state decay kinetics from the TAS global analysis, despite the difference in fluence. Note that the kinetics at 1628 cm^{-1} (within the broad 1620–1660 cm^{-1} ESA region) were also checked to minimise contamination from the GSB, but have very similar lifetime components of 1 and 12 ps (Figure S20, Supporting Information; Table 1). The implication of the matching TAS and PDI C═O stretch decay kinetics is that the singlet exciton is localised on the PDI core of anti-PDFC. This is entirely consistent with TD-DFT calculations performed for anti-PDFC, for which the S_1 state shows a localization of electron density on the PDI core (Figure S21, Supporting Information).

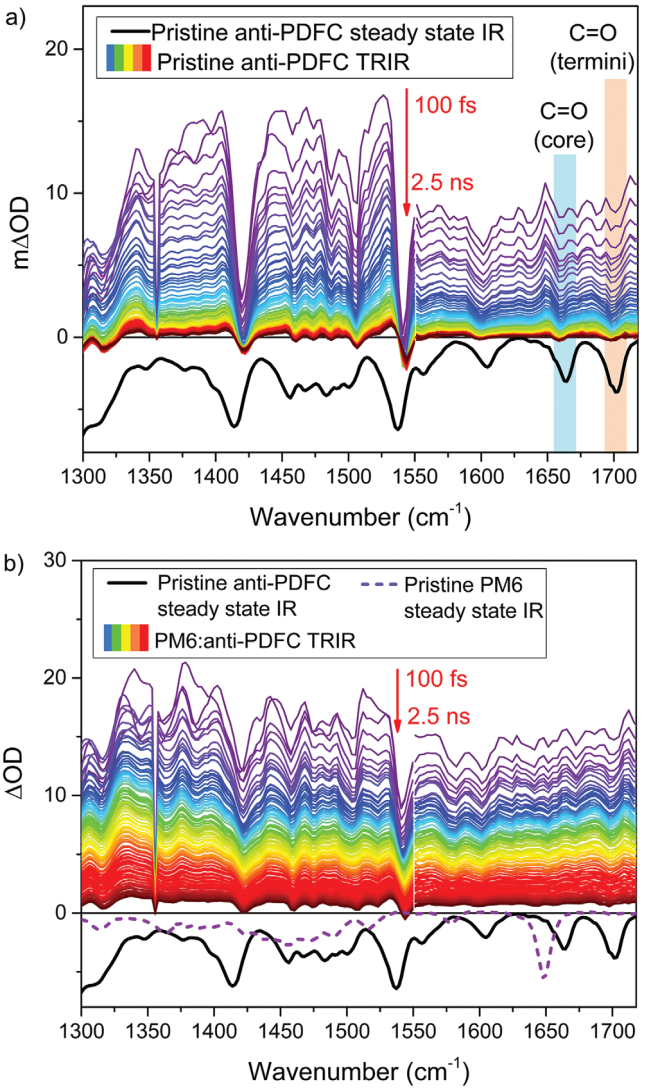

Figure 3. The raw TRIR spectra for a) pristine anti-PDFC and b) PM6:anti-PDFC films. Note that the sharp feature at 1355 cm^{-1} is an artifact. This data was measured using 520 nm and 5 mW excitation, using a higher excitation energy here to demonstrate the transient features.

The two pristine anti-PDFC vibrational modes relating to the terminal 2FIC units (2221 cm^{-1} and 1602 cm^{-1}, Figure 4b) show a greater signal amplitude on nanosecond timescales compared to the anti-PDFC's PDI core C═O stretch ESA at 1648 cm^{-1}. It is known from global analysis of the ps-TAS that charge carriers are observed in pristine anti-PDFC, and that no contribution from triplet states was detected. The larger TRIR signal amplitude on longer timescales for the terminal 2FIC modes therefore suggests that the anion is mostly localised on these terminal 2FIC units.

The localization of the anion on the 2FIC terminal units in pristine anti-PDFC is a significant finding, and thus it is important to assess whether the same occurs in the blend (Figure 4c,d). TRIR of a two-component blend system is even more complex than the pristine acceptor, owing to the spectral congestion that arises from overlap of the PM6 and anti-PDFC GSB/ESA

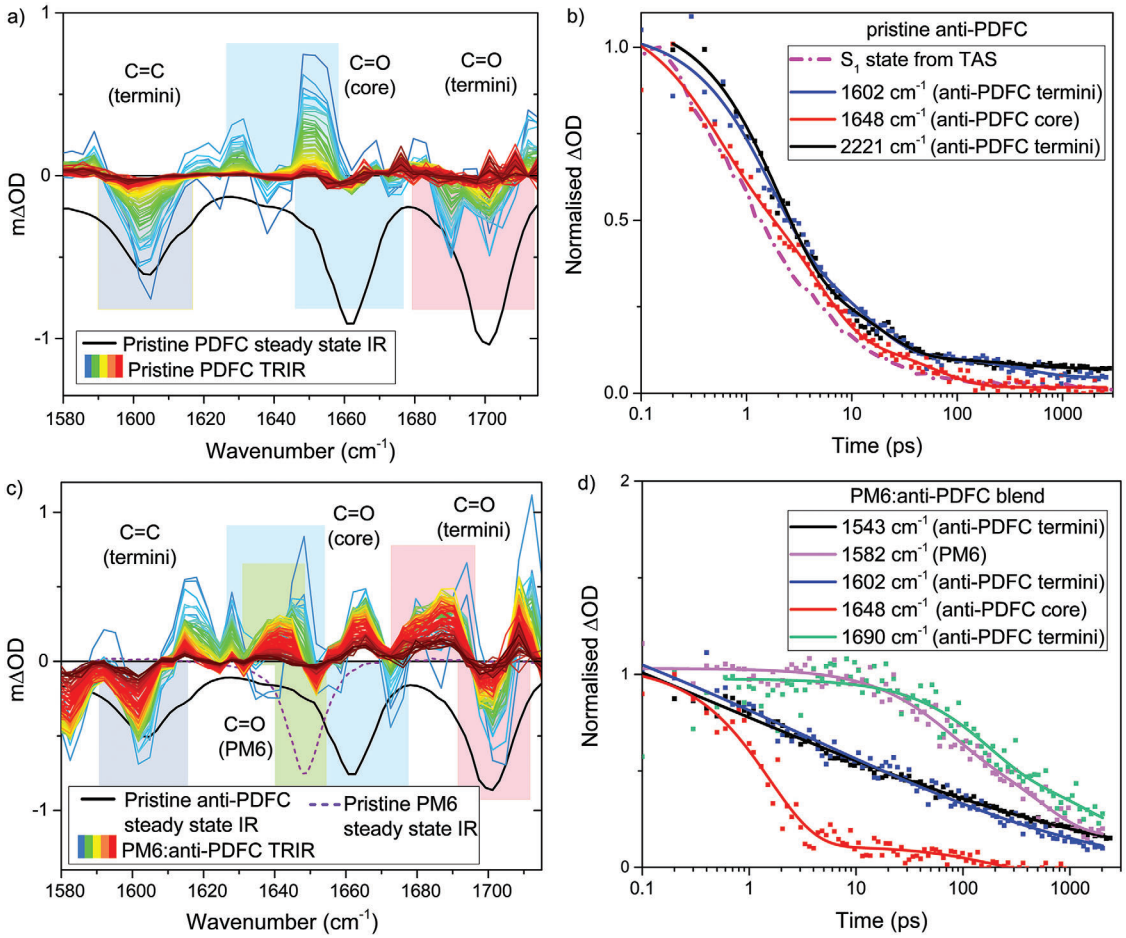

Figure 4. The baselined TRIR spectra, zoomed into the main area of interest, and kinetics (extracted from the baselined spectra) at relevant wavenumbers for a,b) pristine anti-PDFC and c,d) PM6:anti-PDFC films. All data were measured using 520 nm and 1 mW excitation.

vibrational features (the steady state IR spectra for both PM6 and anti-PDFC are included in Figures 3b and 4c). The 1648 cm^{-1} ESA of the blend's anti-PDFC PDI core possesses slower kinetics compared to the pristine anti-PDFC, with lifetime components of 1.5 and 100 ps for the blend versus 0.8 and 14 ps for the pristine anti-PDFC. The ESA at 1628 cm^{-1}–further removed from the bleaches–shows very similar behaviour to 1648 cm^{-1}, consistent with them being part of the same broad ESA feature. This evidence for a longer-lived anti-PDFC singlet exciton in the blend was also observed in the TAS data, and is consistent with a singlet energy transfer process from the PM6 to the anti-PDFC. Furthermore, there is little evidence of a long-lived component in the

Table 1. Wavenumber of selected TRIR GSBs and ESAs, their assignments, and decay time constants.

Wavenumber [cm^{-1}]	Type	Material	Mode	Time constants, [ps]	
				Pristine	Blend
1526	ESA	Anti-PDFC	2FIC terminal C=C	2, 20	[a]
1543	GSB	Anti-PDFC	2FIC terminal C=C	2, 28	15[b]
1602	GSB	Anti-PDFC	2FIC benzene	2, 25	17[b]
1628	ESA	Anti-PDFC	C=O on PDI core	1, 12	2, 100
1648	ESA	Anti-PDFC	C=O on PDI core	0.8, 14	1.5, 100
1690	ESA	Anti-PDFC	C=O on 2FIC termini	[c]	110, 1000
2221	GSB	Anti-PDFC	C≡N on 2FIC termini	2, 25	12[b]
1347	ESA	PM6	Thiophene-BDT	[c]	90, 910
1582	GSB	PM6	Asymmetric thiophene	[c]	90, 850

[a] Overlaps PM6 GSB; [b] Denotes stretch exponential fit; [c] Very weak.

1648 cm^{-1} and 1628 cm^{-1} kinetics (certainly compared to other vibrational modes we assess) and thus are likely to correspond to the PDFC singlet exciton once again. As such, it appears that the anti-PDFC singlet exciton remains localised on the PDI core in the blend.

In the same C═O region (Figure 4c), a much stronger, long-lived ESA at 1690 cm^{-1} is observed for the second anti-PDFC CO stretch (GSB at 1700 cm^{-1}) of the blend, which was much less apparent in the pristine anti-PDFC. Note that no PM6 vibrational modes occur above 1650 cm^{-1} (Figure S22, Supporting Information). Although the DFT calculations suggest this 1700 cm^{-1} mode contains a contribution from the PDI C═O stretches in anti-PDFC, most of the vibrational motion relates to the terminal 2FIC C═O stretches. Furthermore, while a weak GSB has been previously reported in PDI in this spectral region, no ESA accompanied it.[45,46] This observation helps support the assignment of the 1690 cm^{-1} ESA in PM6:anti-PDFC to a terminal 2FIC C═O stretch. The long-lived nature of this ESA (lifetime components of 110 and 1000 ps) indicates it is likely to be assigned to the anti-PDFC radical anion. Furthermore, the observation of a greater intensity of this ESA relative to the pristine film reflects the greater charge carrier populations present in the blend and is thus also consistent with the anion assignment. These points provide evidence that even in the blend, the anion is localised on the terminal 2FIC units.

Other marker modes for the anti-PDFC termini include the 1602 cm^{-1} GSB (fluorinated benzene stretch), 1543 cm^{-1} GSB (C═C stretch linker to termini), and 2221 cm^{-1} CN stretch GSB. Note that these have been specifically chosen because of the lack of PM6 steady-state IR features at these frequencies (Figures 3b and 4c). In all three cases, long-lived TRIR signals with very similar stretched exponential kinetics are observed (Figure 4d; Figure S20, Supporting Information). Stretched exponential kinetics ($\Delta OD \propto e^{-t^{\beta}}$) are often observed in organic photovoltaic systems and are usually a signature of a dispersive environment such that multiple lifetimes are present.[47] That being the case, the simplest approximation for the lifetime in the case of stretched exponential kinetics is an evaluation of the time it takes for the signal amplitude to fall to half of its initial value, $t_{1/2}$. The $t_{1/2}$ values determined here for the marker modes of the anti-PDFC termini are ≈15 ps. Interestingly, however, a closer examination of the kinetics shows that these three anti-PDFC termini GSBs in the blend show an immediate, albeit slow, decay, while the previously discussed ESA at 1690 cm^{-1} (C═O stretch on 2FIC termini) shows a delayed decay (lifetime components 110 and 1000 ps). This may be because the GSBs have some contribution from Fano anti-resonance,[48] in which the vibrational transition couples to the underlying electronic absorption. As such, these GSB kinetics may have both singlet exciton and polaron character. Nevertheless, the longer-lived nature of these 2FIC termini modes in the blend still provide additional evidence for the localization of the anti-PDFC anion on the termini.

As further confirmation of the localization of the anti-PDFC singlet exciton on the PDI core and the anion on the termini, we applied the same kinetic model as was employed to analyse the ultrafast TAS. The TRIR kinetic model analysis of the blend is shown in Figure S23 (Supporting Information). First, the kinetic analysis detects very little population of PM6 excitons, and this is consistent with both the ultrafast decay pathways (energy transfer and charge carrier formation) and the above analysis of the raw data. Second, the extracted TRIR component assigned to the anti-PDFC singlet exciton (as known from the application of the same model to the TAS data) shows decay kinetics virtually identical to the 1648 cm^{-1} vibrational mode localised on the PDI core. The long-lived tail from 10–100 ps seen in both raw and extracted data sets is thus due to the presence of the equilibrium between CT states and anti-PDFC singlet excitons. It also further verifies the localization of the anti-PDFC singlet exciton on the PDI core. Finally, the long-lived extracted components from the kinetic model–the CT and charge separated states–show kinetics consistent with the representative 1690 cm^{-1} mode localised on the anti-PDFC termini. Both data sets show a growth in amplitude until a maximum population is reached at ≈10 ps, with the long-lived nature of the 1690 cm^{-1} termini mode correlated primarily with the charge-separated state.

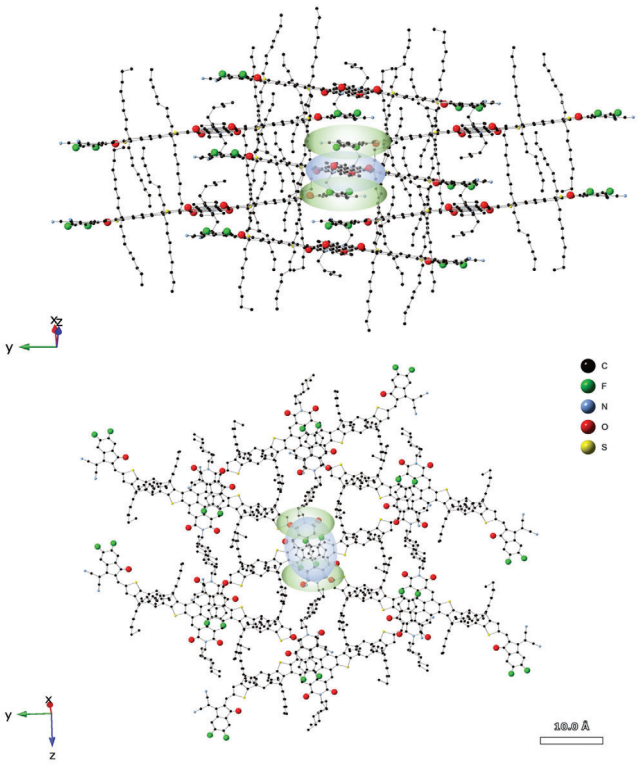

Figure 5. The 3D network of anti-PDFC molecules, established from the single crystal X-ray structure data (side view and top view), showing the localization sites of the singlet exciton (blue) and radical anion (green). This demonstrates the facile electron transfer between the sites and vertical transport channels.

In summary of the TRIR data, it has been observed that, for both pristine and blend films, the anti-PDFC singlet exciton is primarily localised on the PDI central core, while the anion is primarily localised on the 2FIC termini, as demonstrated in **Figure 5**. The crystal structure of pristine anti-PDFC (Figure 1d) has revealed an alternating stacking structure of the terminal units and the PDI core, implying a strong interaction. It is therefore likely that this interaction enables the transfer of the excited electron from the PDI to the 2FIC termini on the adjacent molecule, promoting charge separation and transfer

(Figure 5). We have investigated this interaction further by calculating the electronically excited states of a molecular dimer extracted from the single crystal data, as compared to a monomer, using the Tamm–Dancoff approximation[49] to time-dependent density functional theory and the SVP basis set. These results are presented in Figures S24–S26 and Tables S2 and S3 (Supporting Information). Evidence of strong coupling in the dimer is present as an appreciable 0.11 eV red-shift of the lowest energy electronic transition (compared to the monomer). Furthermore, the singlet state splitting S_2-S_1 gap in the dimer is 0.08 eV, suggesting electronic coupling on the order of 40 meV ($[S_2\text{-}S_1]/2$). Finally, the lowest energy electronic transition in the dimer has strong CT character, with its concomitant low oscillator strength. The calculation shows that the excited electron transitions from the PDI core to the terminal group (Figure S26, Supporting Information), as was also evident in the TRIR data. The difference in Mulliken densities indicates a transfer of 0.90 electrons: a highly efficient charge transfer process.

2.6. Photovoltaic Device Characterization

The observation of anion localization on the 2FIC terminal units of the anti-PDFC NFA is highly significant, and we now turn to the device characteristics to explore the ramifications on charge carrier transport (Figure S27, Supporting Information). To investigate the photovoltaic performance of the PM6:anti-PDFC blend system with different active layer thickness, organic photovoltaic devices were fabricated under a controlled N_2 environment using inverted architecture (glass/ITO/ZnO/active layer/MoO_3/Ag). The detailed fabrication procedure can be found in the experimental section. Current density-voltage (J-V) curves under AM1.5G illumination (Figure S27a, Supporting Information) show that a high fill factor of 73% is present, with efficiency of 14.8%. The devices showed maximum external quantum efficiencies over 80% with an integrated current of 19 mA cm^{-2} (Figure S28, Supporting Information). The J-V behaviour under different light intensities is discussed in the supporting information (Figures S29 and S30, Supporting Information).

High fill factors, especially with thick active layers, are usually associated with non-Langevin bimolecular recombination and long-lived charge carriers. However, this is clearly not the case for PM6:anti-PDFC, for which the TAS shows little evidence of bimolecular recombination and relatively few charges still exist on µs timescales. Indeed, given the rapid geminate recombination observed, it is remarkable that device efficiencies of over 14% and fill factor values of over 70% are measured, noting that fill factors of over 80% have been previously reported[20] for the PM6:anti-PDFC blend. This likely has origins in efficient charge transport.

To probe charge carrier extraction of PM6:anti-PFDC devices, we carried out transient photocurrent measurements (Figure S27b, Supporting Information). A very fast extraction time of 1.5 µs is observed, substantially faster than other "benchmark systems" like P3HT:PCBM,[50] and similar to state-of-the-art systems such as PM6:Y6.[51,52] The extremely rapid extraction of charge carriers in PM6:anti-PDFC agrees with the very high fill factor observed. Since the TAS experiments showed relatively rapid charge carrier recombination, this implies that charge extraction competes very effectively with the recombination in these devices, enabling the high fill factor.[53] Furthermore, because the perpendicular alkyl chains of anti-PDFC impose a rigid 3D reticular structure that facilitates aligned stacking of the termini and the PDI units,[21] this will create an effective charge transport channel[54] for the termini-localised anions, facilitating the rapid charge extraction observed. Indeed, given that the 2FIC terminal unit is very common amongst high-performing NFAS, and noting that in-depth morphology studies of many similar 2FIC-terminated NFAs show π–π stacking between the termini,[55,56] this anion localization and resultant effective electron transport is likely present in other NFA-based OPV systems as a significant contributor to the high device performances observed.

3. Conclusion

A high-performing non-fullerene acceptor, anti-PDFC, has been investigated in both pristine films and in blends with PM6. A variety of spectroscopic and morphology characterization techniques have been employed to investigate the links between excited state dynamics and molecular structure. Both steady state spectroscopy and morphology reveal that the crystallinity of the NFA in the pristine film is maintained in the blend. A combination of spectroelectrochemistry and microsecond transient absorption spectroscopy provided control spectra of pertinent excited states: the polymer cation, anti-PDFC anion, and both triplet states. These were used to analyse ps-TAS data, which demonstrated several important factors: very fast charge carrier recombination, extension of the anti-PDFC singlet lifetime (via an exciton-CT state equilibrium and singlet energy transfer), and a close similarity of the charge carrier recombination in both pristine NFA and blend films, attributed to recombination within the pristine domains dominating. Most significantly, analysis of ultrafast time-resolved infrared spectroscopy data of both the pristine anti-PDFC and the PM6:anti-PDFC blend showed that the anti-PDFC singlet is localised on the PDI core but the radical anion is correlated much more strongly with vibrational modes localised on the 2FIC termini. This shift is correlated with a close interaction between the termini and the PDI core, facilitating the electron transfer. Furthermore, the very rapid charge extraction measured for PM6:anti-PDFC photovoltaic devices may also be correlated with the anion localization enabling effective charge transport channels. Given the prevalence of the 2FIC terminal group in the highest-performing non-fullerene acceptors to date, such as the Y6 family, this observation may offer a unique insight into why such materials perform so well in organic photovoltaics.

Supporting Information

Supporting Information is available from the Wiley Online Library or from the author.

Acknowledgements

The authors acknowledge the Optoelectronics Group at the University of Cambridge for sharing the software for global analysis and Professor James Durrant for providing access to spectroelectrochemistry instrumentation. T.M.C. would like to acknowledge support from EPSRC project EP/N026411/1. Both T.M.C. and H.Z. thank the SJTU Global Strategic Partnership Fund. J.A.W. thanks the STFC for an award of the experimental time

(ULTRA experiment #22230032), the EPSRC for a capital award to the Lord Porter Laser Laboratory at Sheffield, and the Grantham Centre for Sustainable Futures (PhD funding for M.V.A. and J.D.S.). J.A.W. is grateful to the Royal Society for the Leverhulme Senior Research Fellowship. Z.Q and N.G. acknowledge financial support from the UK EPSRC through the ATIP Programme Grant (EP/T028513/1) and the King Abdullah University of Science and Technology (KAUST) Office of Sponsored Research (OSR under Award ORFS-2023-OFP-5544. R.J.F.-T. acknowledges financial support from the Swiss National Science Foundation through an Early Postdoc Mobility grant (P2ZHP2-199422) and from the University of Geneva, and also thanks the University of Geneva for computational support through the use of the Yggdrasil and Baobab HPC Clusters. T.S. would like to thank the National Natural Science Foundation of China (Grant no. 62204154) for providing the funding. R.C.O. acknowledges the use of the UCL High Performance Computing Facility Myriad@UCL. M.V.A has received funding from the European Union's Horizon 2020 research and innovation program under the Marie Skłodowska-Curie grant agreement No 884104 (PSI-FELLOW-III-3i).

Conflict of Interest

The authors declare no conflict of interest.

Data Availability Statement

The data that support the findings of this study are available from the corresponding author upon reasonable request.

Keywords

non-fullerene acceptors, organic photovoltaics, time-resolved infrared spectroscopy, transient absorption spectroscopy

Received: October 23, 2024
Revised: December 13, 2024
Published online:

[1] L. Zhu, M. Zhang, J. Xu, C. Li, J. Yan, G. Zhou, W. Zhong, T. Hao, J. Song, X. Xue, Z. Zhou, R. Zeng, H. Zhu, C.-C. Chen, R. C. I. MacKenzie, Y. Zou, J. Nelson, Y. Zhang, Y. Sun, F. Liu, *Nat. Mater.* **2022**, *21*, 656.
[2] C. Han, J. Wang, S. Zhang, L. Chen, F. Bi, J. Wang, C. Yang, P. Wang, Y. Li, X. Bao, *Adv. Mater.* **2023**, *35*, 2208986.
[3] Y. Jiang, S. Sun, R. Xu, F. Liu, X. Miao, G. Ran, K. Liu, Y. Yi, W. Zhang, X. Zhu, *Nat. Energy* **2024**, *9*, 975.
[4] A. Armin, W. Li, O. J. Sandberg, Z. Xiao, L. Ding, J. Nelson, D. Neher, K. Vandewal, S. Shoaee, T. Wang, H. Ade, T. Heumüller, C. Brabec, P. Meredith, *Adv. Energy Mater.* **2021**, *11*, 2003570.
[5] W. Lowrie, R. J. E. Westbrook, J. Guo, H. I. Gonev, J. Marin-Beloqui, T. M. Clarke, *J. Chem. Phys.* **2023**, *158*, 110901.
[6] J. Liu, S. Chen, D. Qian, B. Gautam, G. Yang, J. Zhao, J. Bergqvist, F. Zhang, W. Ma, H. Ade, O. Inganäs, K. Gundogdu, F. Gao, H. Yan, *Nat. Energy* **2016**, *1*, 16089.
[7] Y. Zhong, M. Causa', G. J. Moore, P. Krauspe, B. Xiao, F. Günther, J. Kublitski, R. Shivhare, J. Benduhn, E. BarOr, S. Mukherjee, K. M. Yallum, J. Réhault, S. C. B. Mannsfeld, D. Neher, L. J. Richter, D. M. DeLongchamp, F. Ortmann, K. Vandewal, E. Zhou, N. Banerji, *Nat. Comm.* **2020**, *11*, 833.
[8] L. Perdigón-Toro, H. Zhang, A. Markina, J. Yuan, S. M. Hosseini, C. M. Wolff, G. Zuo, M. Stolterfoht, Y. Zou, F. Gao, D. Andrienko, S. Shoaee, D. Neher, *Adv. Mater.* **2020**, *32*, 1906763.
[9] S. Karuthedath, J. Gorenflot, Y. Firdaus, N. Chaturvedi, C. S. P. De Castro, G. T. Harrison, J. I. Khan, A. Markina, A. H. Balawi, T. A. D. Peña, W. Liu, R.-Z. Liang, A. Sharma, S. H. K. Paleti, W. Zhang, Y. Lin, E. Alarousu, D. H. Anjum, P. M. Beaujuge, S. De Wolf, I. McCulloch, T. D. Anthopoulos, D. Baran, D. Andrienko, F. Laquai, *Nat. Mater.* **2021**, *20*, 378.
[10] B. Schweda, M. Reinfelds, P. Hofstadler, G. Trimmel, T. Rath, *ACS Appl. Energy Mater.* **2021**, *4*, 11899.
[11] S. Feng, M. Li, N. Tang, X. Wang, H. Huang, G. Ran, Y. Liu, Z. Xie, W. Zhang, Z. Bo, *ACS Appl. Mater. Interfaces* **2020**, *12*, 4638.
[12] T. J. Aldrich, M. Matta, W. Zhu, S. M. Swick, C. L. Stern, G. C. Schatz, A. Facchetti, F. S. Melkonyan, T. J. Marks, *JACS* **2019**, *141*, 3274.
[13] S. Dai, F. Zhao, Q. Zhang, T.-K. Lau, T. Li, K. Liu, Q. Ling, C. Wang, X. Lu, W. You, X. Zhan, *JACS* **2017**, *139*, 1336.
[14] C. Yao, Y. Yang, L. Li, M. Bo, J. Zhang, C. Peng, Z. Huang, J. Wang, *J. Phys. Chem. C* **2020**, *124*, 23059.
[15] S. E. Bailey, J. S. Cohan, J. I. Zink, *J. Phys. Chem. B.* **2000**, *104*, 10743.
[16] R. D. Pensack, J. B. Asbury, *JACS* **2009**, *131*, 15986.
[17] S. M. Falke, C. A. Rozzi, D. Brida, M. Maiuri, M. Amato, E. Sommer, A. De Sio, A. Rubio, G. Cerullo, E. Molinari, C. Lienau, *Science* **2014**, *344*, 1001.
[18] F. Provencher, N. Bérubé, A. W. Parker, G. M. Greetham, M. Towrie, C. Hellmann, M. Côté, N. Stingelin, C. Silva, S. C. Hayes, *Nat. Comm.* **2014**, *5*, 4288.
[19] K. Pagano, J. G. Kim, J. Luke, E. Tan, K. Stewart, I. V. Sazanovich, G. Karras, H. I. Gonev, A. V. Marsh, N. Y. Kim, S. Kwon, Y. Y. Kim, M. I. Alonso, B. Dörling, M. Campoy-Quiles, A. W. Parker, T. M. Clarke, Y.-H. Kim, J.-S. Kim, *Nat. Comm.* **2024**, *15*, 6153.
[20] K. Ding, T. Shan, J. Xu, M. Li, Y. Wang, Y. Zhang, Z. Xie, Z. Ma, F. Liu, H. Zhong, *Chem. Commun.* **2020**, *56*, 11433.
[21] T. Shan, K. Ding, L. Yu, X. Wang, Y. Zhang, X. Zheng, C.-C. Chen, Q. Peng, H. Zhong, *Adv. Funct. Mater.* **2021**, *31*, 2100750.
[22] J. Fang, Z. Wang, Y. Chen, Q. Zhang, J. Zhang, L. Zhu, M. Zhang, Z. Cui, Z. Wei, H. Ade, C.-Q. Ma, *Cell Rep. Phys. Sci.* **2022**, *3*, 100983.
[23] T. M. Clarke, A. M. Ballantyne, J. Nelson, D. D. C. Bradley, J. R. Durrant, *Adv. Funct. Mater.* **2008**, *18*, 4029.
[24] F. C. Spano, *Acc. Chem. Res.* **2010**, *43*, 429.
[25] R. Hou, M. Li, X. Ma, H. Huang, H. Lu, Q. Jia, Y. Liu, X. Xu, H.-B. Li, Z. Bo, *ACS Appl. Mater. Interfaces* **2020**, *12*, 46220.
[26] G. Li, F. Qin, R. M. Jacobberger, S. Mukherjee, L. O. Jones, R. M. Young, R. M. Pankow, B. P. Kerwin, L. Q. Flagg, D. Zheng, L.-W. Feng, K. L. Kohlstedt, V. K. Sangwan, M. C. Hersam, G. C. Schatz, D. M. DeLongchamp, M. R. Wasielewski, Y. Zhou, A. Facchetti, T. J. Marks, *Joule* **2023**, *7*, 2152.
[27] S. S. Batsanov, *Inorg. Mater.* **2001**, *37*, 871.
[28] H. Bristow, K. J. Thorley, A. J. P. White, A. Wadsworth, M. Babics, Z. Hamid, W. Zhang, A. F. Paterson, J. Kosco, J. Panidi, T. D. Anthopoulos, I. McCulloch, *Adv. Electron. Mater.* **2019**, *5*, 1900344.
[29] G. Zhang, X.-K. Chen, J. Xiao, P. C. Y. Chow, M. Ren, G. Kupgan, X. Jiao, C. C. S. Chan, X. Du, R. Xia, Z. Chen, J. Yuan, Y. Zhang, S. Zhang, Y. Liu, Y. Zou, H. Yan, K. S. Wong, V. Coropceanu, N. Li, C. J. Brabec, J.-L. Bredas, H.-L. Yip, Y. Cao, *Nat. Comm.* **2020**, *11*, 3943.
[30] C. Xiao, C. Li, F. Liu, L. Zhang, W. Li, *J. Mater. Chem. C* **2020**, *8*, 5370.
[31] J. Guo, B. Moss, T. M. Clarke, *J. Mater. Chem. A* **2022**, *10*, 20874.
[32] T. F. Hinrichsen, C. C. S. Chan, C. Ma, D. Paleček, A. Gillett, S. Chen, X. Zou, G. Zhang, H.-L. Yip, K. S. Wong, R. H. Friend, H. Yan, A. Rao, P. C. Y. Chow, *Nat. Comm.* **2020**, *11*, 5617.
[33] Y. Wang, J. Luke, A. Privitera, N. Rolland, C. Labanti, G. Londi, V. Lemaur, D. T. W. Toolan, A. J. Sneyd, S. Jeong, D. Qian, Y. Olivier, L. Sorace, J.-S. Kim, D. Beljonne, Z. Li, A. J. Gillett, *Joule* **2023**, *7*, 810.
[34] A. J. Gillett, A. Privitera, R. Dilmurat, A. Karki, D. Qian, A. Pershin, G. Londi, W. K. Myers, J. Lee, J. Yuan, S.-J. Ko, M. K. Riede, F. Gao, G. C. Bazan, A. Rao, T.-Q. Nguyen, D. Beljonne, R. H. Friend, *Nature* **2021**, *597*, 666.

[35] R. Wang, C. Zhang, Q. Li, Z. Zhang, X. Wang, M. Xiao, *JACS* **2020**, *142*, 12751.
[36] L. Perdigón-Toro, L. Q. Phuong, S. Zeiske, K. Vandewal, A. Armin, S. Shoaee, D. Neher, *ACS Energy Lett.* **2021**, *6*, 557.
[37] Y. Zhang, M. T. Sajjad, O. Blaszczyk, A. Ruseckas, L. A. Serrano, G. Cooke, I. D. W. Samuel, *Org. Electron.* **2019**, *70*, 162.
[38] J. M. Marin-Beloqui, D. T. W. Toolan, N. A. Panjwani, S. Limbu, J.-S. Kim, T. M. Clarke, *Adv. Energy Mater.* **2021**, *11*, 2100539.
[39] J. M. Carr, T. G. Allen, B. W. Larson, I. G. Davydenko, R. R. Dasari, S. Barlow, S. R. Marder, O. G. Reid, G. Rumbles, *Mater. Horiz.* **2022**, *9*, 312.
[40] A. Karki, J. Vollbrecht, A. J. Gillett, P. Selter, J. Lee, Z. Peng, N. Schopp, A. L. Dixon, M. Schrock, V. Nádaždy, F. Schauer, H. Ade, B. F. Chmelka, G. C. Bazan, R. H. Friend, T.-Q. Nguyen, *Adv. Energy Mater.* **2020**, *10*, 2001203.
[41] K. Nakano, Y. Chen, B. Xiao, W. Han, J. Huang, H. Yoshida, E. Zhou, K. Tajima, *Nat. Comm.* **2019**, *10*, 2520.
[42] R. J. Fernández-Terán, E. Sucre-Rosales, L. Echevarria, F. E. Hernández, *J. Chem. Educ.* **2022**, *99*, 2327.
[43] C. M. Mauck, R. M. Young, M. R. Wasielewski, *J. Phys. Chem. A* **2017**, *121*, 784.
[44] N. Pearce, K. E. A. Reynolds, S. Kayal, X. Z. Sun, E. S. Davies, F. Malagreca, C. J. Schürmann, S. Ito, A. Yamano, S. P. Argent, M. W. George, N. R. Champness, *Nat. Comm.* **2022**, *13*, 415.
[45] E. R. Kennehan, C. Grieco, A. N. Brigeman, G. S. Doucette, A. Rimshaw, K. Bisgaier, N. C. Giebink, J. B. Asbury, *Phys. Chem. Chem. Phys.* **2017**, *19*, 24829.
[46] P. E. Hartnett, C. M. Mauck, M. A. Harris, R. M. Young, Y.-L. Wu, T. J. Marks, M. R. Wasielewski, *JACS* **2017**, *139*, 749.
[47] J. Guo, J. M. Marin-Beloqui, T. M. Clarke, *J. Phys. Mater.* **2021**, *4*, 044009.
[48] W. J. Kendrick, M. Jirásek, M. D. Peeks, G. M. Greetham, I. V. Sazanovich, P. M. Donaldson, M. Towrie, A. W. Parker, H. L. Anderson, *Chem. Sci.* **2020**, *11*, 2112.
[49] S. Hirata, M. Head-Gordon, *Chem. Phys. Lett.* **1999**, *314*, 291.
[50] R. C. I. MacKenzie, C. G. Shuttle, M. L. Chabinyc, J. Nelson, *Adv. Energy Mater.* **2012**, *2*, 662.
[51] S. Alam, H. Aldosari, C. E. Petoukhoff, T. Váry, W. Althobaiti, M. Alqurashi, H. Tang, J. I. Khan, V. Nádaždy, P. Müller-Buschbaum, G. C. Welch, F. Laquai, *Adv. Funct. Mater.* **2024**, *34*, 2308076.
[52] N. Yao, J. Wang, Z. Chen, Q. Bian, Y. Xia, R. Zhang, J. Zhang, L. Qin, H. Zhu, Y. Zhang, F. Zhang, *J. Phys. Chem. Lett.* **2021**, *12*, 5039.
[53] D. Bartesaghi, I. d. C. Pérez, J. Kniepert, S. Roland, M. Turbiez, D. Neher, L. J. A. Koster, *Nat. Comm.* **2015**, *6*, 7083.
[54] L. Ye, K. Weng, J. Xu, X. Du, S. Chandrabose, K. Chen, J. Zhou, G. Han, S. Tan, Z. Xie, Y. Yi, N. Li, F. Liu, J. M. Hodgkiss, C. J. Brabec, Y. Sun, *Nat. Comm.* **2020**, *11*, 6005.
[55] G. Han, Y. Guo, X. Song, Y. Wang, Y. Yi, *J. Mater. Chem. C* **2017**, *5*, 4852.
[56] P. Mondelli, P. Kaienburg, F. Silvestri, R. Scatena, C. Welton, M. Grandjean, V. Lemaur, E. Solano, M. Nyman, P. N. Horton, S. J. Coles, E. Barrena, M. Riede, P. Radaelli, D. Beljonne, G. N. M. Reddy, G. Morse, *J. Mater. Chem. A* **2023**, *11*, 16263.